CORA Cork Open Research Archive
Cartlann Taighde Oscailte Chorcaí

Title	GaAs MMIC nonreciprocal single-band, multi-band, and tunable bandpass filters
Authors	Simpson, Dakotah;Psychogiou, Dimitra
Publication date	2023-01-02
Original Citation	Simpson, D. and Psychogiou, D. (2023) 'GaAs MMIC nonreciprocal single-band, multi-band, and tunable bandpass filters', IEEE Transactions on Microwave Theory and Techniques, 71(6), pp.2439-2449. https://doi.org/10.1109/TMTT.2022.3232103
Type of publication	Article (peer-reviewed)
Link to publisher's version	10.1109/TMTT.2022.3232103
Rights	© 2023, IEEE. Personal use of this material is permitted. Permission from IEEE must be obtained for all other uses, in any current or future media, including reprinting/republishing this material for advertising or promotional purposes, creating new collective works, for resale or redistribution to servers or lists, or reuse of any copyrighted component of this work in other works.
Download date	2026-11-07 08:16:04
Item downloaded from	https://hdl.handle.net/10468/14220

UCC
University College Cork, Ireland
Coláiste na hOllscoile Corcaigh

This article has been accepted for inclusion in a future issue of this journal. Content is final as presented, with the exception of pagination.

GaAs MMIC Nonreciprocal Single-Band, Multi-Band, and Tunable Bandpass Filters

Dakotah Simpson, *Member, IEEE*, and Dimitra Psychogiou, *Senior Member, IEEE*

***Abstract*— This article reports on the RF design and practical development of active MMIC single-band, multi-band, and tunable bandpass filters (BPFs) with lossless and nonreciprocal transfer functions. They are based on series-cascaded lumped-element frequency-selective cells that are coupled with MMIC-based FETs. The FETs introduce gain and counteract the loss of the lossy elements. Furthermore, due to their unilateral behavior, nonreciprocal transfer functions can be obtained. This allows for an RF codesigned filtering isolator functionality to be created within a single RF component. By cascading multiple frequency-selective cells, both single-band and multi-band transfer functions with and without transmission zeros (TZs) can be realized. The basic operating principles of the MMIC concept are first described through parametric studies on different types of frequency-selective cells. These are followed by tunable and higher selectivity design methodologies. For practical demonstration purposes, four MMIC prototypes were designed, built, and measured using a commercially available GaAs process. They include a three-cell frequency-tunable BPF, two dual-band BPFs, and a quasi-elliptic BPF.**

***Index Terms*— Active filter, bandpass filter (BPF), GaAs, MMIC, multi-band filter, nonreciprocal, tunable filter.**

I. Introduction

IN CONTEMPORARY RF and microwave systems, the use of large form-factor RF filtering technologies based on PCB-based microstrip, coupled lines, or waveguide-based architectures is a common practice due to their medium-to-high quality factors (Q) and relatively low insertion loss (IL). However, these types of filters cannot be directly integrated nor can be codesigned with other front-end devices such as amplifiers, mixers, or isolators since these are typically built using integrated circuit (IC) processes such as GaAs, Si, or GaN. Codesigned bandpass filters (BPFs) and isolators have the potential to reduce the size and improve the performance of RF front-ends by combining the two RF signal processing actions within the volume of a single device. They find application in instrumentation and radar systems and other systems where reflections need to be canceled. In full-duplex systems where the same frequency is being used for transmit and receive, codesigned BPF-isolators can be used as an isolation element between the channels, thus improving their performance.

As the size requirements of RF front ends continually grow stricter, recent research efforts are geared toward monolithic microwave integrated circuit (MMIC)-based design approaches as a way to minimize their size and to integrate them with other RF front-end active and nonlinear devices [1], [2], [3], [4], [5], [6], [9], [10], [11], [12], [13], [14], [15], [16], [17], [18], [19], [20], [21], [22], [23], [24]. However, initial MMIC passive component-based design efforts have led to lossy BPF configurations or to BPFs with ultrawideband passband bandwidth [2], [3], [4], [5], [6]. A plethora of active IC-based BPF concepts has arisen within the past two decades in order to combat the loss of the passive components [6], [11], [12], [13], [14], [15], [16], [17], [18], [19], [20], [21], [22], [23], [24]. These include cascaded filter-amplifier configurations [6], [11], recursive filters [12], [13], [14], active component or negative resistance filters [15], [16], [17], [18], [19], [20], and actively coupled filters [21], [22], [23], [24].

In cascaded filter-amplifier configurations, conventional lossy filters are cascaded with amplifier gain stages [6], [11]. The main drawback of this architecture is that it requires two separate circuits, one for the filtering and one for gain, leading to a larger overall device size. Although this method is simple, it adds gain to the entire lossy response as opposed to adding gain to the individual resonators, which results in transfer function rounding and mismatch loss.

Recursive filters are based on an approach that was initially used in digital filter design methods where a time-delayed, active feedback path is added to the forward path to introduce gain [12], [13], [14]. Besides having a complex and highly sensitive design, these filters have also shown other limitations. The recursive filter in [12] results in poor passband flatness and low selectivity, which can only be remedied by channelizing the filter and including two more filter paths. The filter in [14] is based on a subclass of recursive filters known as transversal filters. Despite showing a selective response with two TZs, the filter is not matched—in-band return loss (RL) that reaches 7 dB—and there is still 2 dB of IL in the passband.

Active and negative resistance filters counteract the loss of passive components by using transistors that introduce gain

Manuscript received 7 June 2022; revised 22 November 2022; accepted 11 December 2022. This work was supported in part by the National Science Foundation (NSF) under Grant ECCS-1941315. Aspects of this work were also supported by the Science Foundation Ireland (SFI) under Grant 20/RP/8334. *(Corresponding author: Dakotah Simpson.)*

Dakotah Simpson was with the Department of Electrical, Computer, and Energy Engineering, University of Colorado Boulder, Boulder, CO 80309 USA. He is now with Lockheed Martin Corporation, Littleton, CO 80127 USA (e-mail: dakotah.simpson@colorado.edu).

Dimitra Psychogiou is with the Department of Electrical and Electronic Engineering, University College Cork, Cork 021, T12 K8AF Ireland, and also with the Tyndall National Institute, Cork, T12 R5CP, Ireland (e-mail: dpsychogiou@ucc.ie).

Color versions of one or more figures in this article are available at https://doi.org/10.1109/TMTT.2022.3232103.

Digital Object Identifier 10.1109/TMTT.2022.3232103

0018-9480 © 2023 IEEE. Personal use is permitted, but republication/redistribution requires IEEE permission.
See https://www.ieee.org/publications/rights/index.html for more information.

Authorized licensed use limited to: UNIVERSITY COLLEGE CORK. Downloaded on February 07,2023 at 16:36:24 UTC from IEEE Xplore. Restrictions apply.

This article has been accepted for inclusion in a future issue of this journal. Content is final as presented, with the exception of pagination.

at the source of loss [15], [16], [17], [18], [19], [20]. One example of this is an active circuit that introduces gain to a lossy inductor in an *LC* tank resonator. The filter in [15] uses an active inductance in its resonators to make the filter tunable in frequency. However, the active circuit does not introduce gain to the resonator and the response presents high IL levels up to 7.8 dB. Other works are limited to low-order designs (second order in [16] and [17] and first order in [18]).

In actively coupled BPFs, FETs are used as couplings between the passive resonators of the filter. Furthermore, they add gain to the individual resonators [21], [22], [23], [24]. Some of the advantages of this filter topology due to FETs replacing the coupling elements in the filter are a smaller size and simpler design. Furthermore, gain is added directly to the resonators, and there is a potential for the FETs to perform multiple functions since they are in line with the filter path. However, these filters exhibit poor passband flatness and output matching in [21] and [22]. Furthermore, the concept in [23] has not been experimentally validated. Moreover, there has been no mention of applying these concepts to multi-band designs.

To address the aforementioned challenges, this article reports on a new class of single-band, tunable, and multi-band active BPFs that exhibit nonreciprocal transfer functions without IL. The integration of the filters' passive and active components on a GaAs MMIC platform enables size miniaturization and high frequency of operation (X-band). A simple design and implementation methodology using cascaded frequency-selective cells is proposed for a variety of transfer functions (quasi-elliptic, flat passband, multi-band, and so on). The resonant elements are actively coupled together through unilateral FETs that provide gain to the overall response. Different types of resonant elements are used to achieve selective single-band and multi-band responses. RF tuning is also explored by incorporating FET-based varactors in the cells. The rest of this article is organized as follows. In Section II, a cascaded-cell approach is described in detail starting from its conceptual design and continuing to in-depth design methodologies for both single-band and multi-band filters. Section III details four MMIC schematics, their prototypes, and their measurements for experimental validation. Finally, a summary of the contributions of this work is given in Section IV.

II. Theoretical Background

The nonreciprocal active MMIC BPF concept is presented in Fig. 1. Specifically, Fig. 1(a) shows the filter architecture that is comprised of N cascaded frequency-selective cells with individual transfer functions $H_{1-N}(\omega)$. The block diagram of the frequency-selective cell is shown in Fig. 1(b). It consists of a passive lossy resonant element that is cascaded between two common-source FETs. Alternative types of resonant elements can be employed, as shown in Fig. 2. The resonant element is connected to the drain of the first FET and to the gate of the second FET. As such, the overall filter architecture is composed of N passive BPF resonant elements that are coupled to each other and to the RF input and output of the filter through FETs. The conceptual response in Fig. 1(c) shows that the loss of the resonant element is offset by the gain

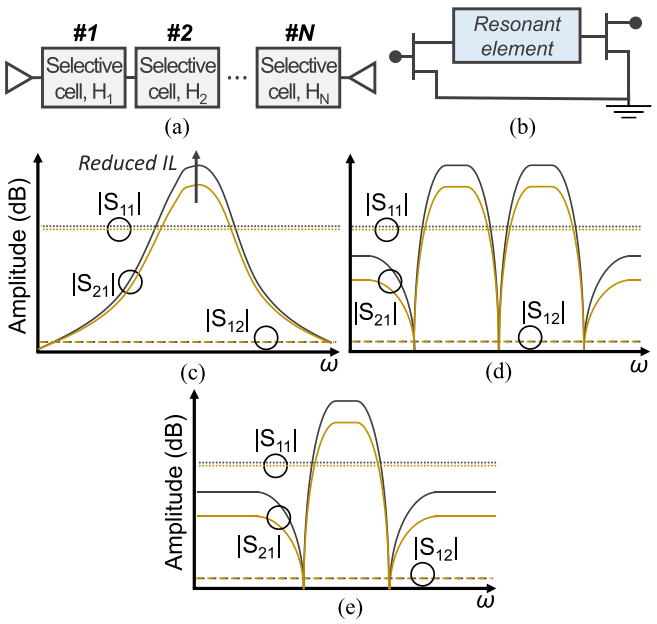


Fig. 1. Actively coupled MMIC BPF concept. (a) BPF architecture made up of a cascade of N frequency-selective cells. (b) Schematic of a frequency-selective cell consisting of two FETs and a resonant element. (c) Conceptual response of an active BPF showing elimination of the IL. (d) Conceptual response of an active dual-band BPF. (e) Conceptual response of a quasi-elliptic BPF.

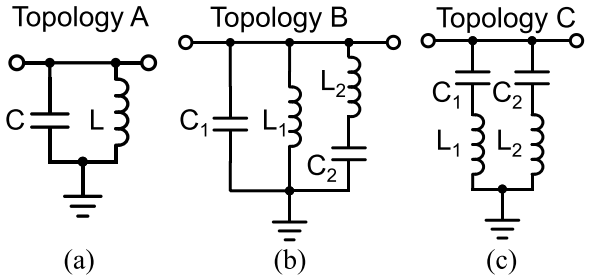


Fig. 2. Resonant elements used within the frequency-selective cells. (a) Topology A: parallel *LC* tank. (b) Topology B: parallel *LC* tank in parallel with a series resonator. (c) Topology C: two series *LC* resonators in parallel with one another.

of the FETs. As a result, a BPF transfer function, $H(\omega)$, with reduced or zero IL can be obtained. Using the other types of elements in Fig. 2 leads to different response types as shown in Fig. 1(d) and (e) for dual-band and quasi-elliptic responses, respectively.

An added benefit of the proposed filter design approach is that the devised filters also operate as nonreciprocal isolators due to the use of FETs, thus exhibiting the RF codesigned functionality of a filter and an isolator. Specifically, the band-pass response is only achieved in one direction of transmission, whereas in the reverse direction, the RF signals are highly rejected. Thus, such an RF performance characteristic can be exploited to miniaturize the RF front-end size through RF components with collocated RF functionalities, which in this case are the function of the BPF and the isolator.

In the following subsections, a thorough design process of the active MMIC BPF concept is outlined, starting with the

Authorized licensed use limited to: UNIVERSITY COLLEGE CORK. Downloaded on February 07,2023 at 16:36:24 UTC from IEEE Xplore. Restrictions apply.

This article has been accepted for inclusion in a future issue of this journal. Content is final as presented, with the exception of pagination.

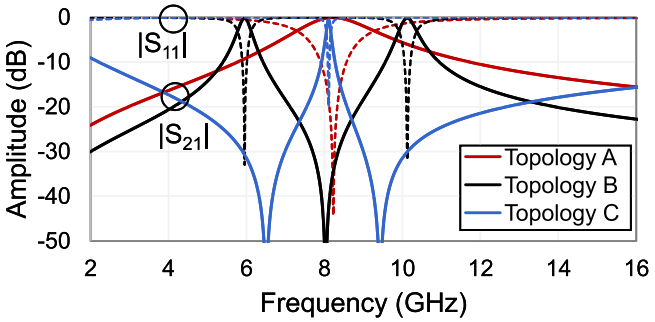


Fig. 3. Transfer functions of the resonant elements in Fig. 2.

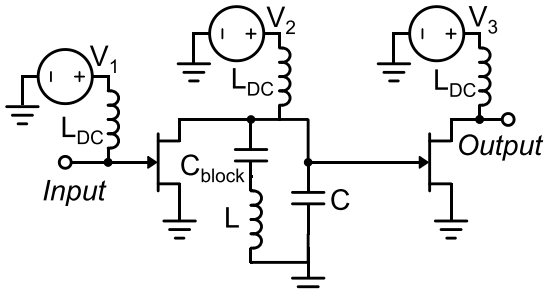


Fig. 4. Circuit schematic of a frequency-selective cell that contains a Topology A resonant element.

compositions and properties of the passive resonant elements. Then, the frequency-selective cell is analyzed in detail. Next, it is shown how these frequency-selective cells are cascaded to develop a BPF. The basic single-band BPF is then extended to higher selectivity and multi-band architectures. Tunability is later added by incorporating varactor diodes in the passive resonant elements. Finally, the design parameters of the MMIC lumped elements are explored.

A. Passive Resonant Elements

Fig. 2 shows a nonexhaustive list of passive resonant elements that can be used within the frequency-selective cells to achieve a variety of frequency-selective transfer functions. Their individual transmission responses are shown in Fig. 3. The simplest resonant element that can be used in the actively coupled filter is the parallel LC tank resonator (Topology A), which is shown in Fig. 2(a). As shown in Fig. 3, this circuit results in one pole at its resonant frequency. The frequency location of the pole is found as follows:

$$\omega_p = \frac{1}{\sqrt{LC}}. \tag{1}$$

Fig. 2(b) shows that the Topology B resonant element consists of an LC tank in parallel with a series LC resonator. It exhibits a dual-band response (one pole in each band) with a transmission zero (TZ) between the two bands. The locations of the poles, $\omega_{p1,2}$, and TZ, ω_{tz}, can be calculated as follows:

$$\omega_{p1,2} = \sqrt{\frac{A+B+C \mp \sqrt{A^2+B^2+C^2+2AC+2BC-2AB}}{2AB}} \tag{2}$$

$$\omega_{tz} = \frac{1}{\sqrt{A}} \tag{3}$$

$$A = L_2C_2 \tag{4}$$

$$B = L_1C_1 \tag{5}$$

$$C = L_1C_2. \tag{6}$$

Fig. 2(c) shows the Topology C resonant element that consists of two series resonators in parallel, which create two TZs and one pole. The series resonators resonate at the frequencies of the TZs, whereas the pole is located in-between them. This circuit is useful to create quasi-elliptic-type transfer functions. The pole and TZs are located according to the following equations, respectively:

$$\omega_p = \sqrt{\frac{C_1+C_2}{C_1C_2(L_1+L_2)}} \tag{7}$$

$$\omega_{tz1} = \frac{1}{\sqrt{L_1C_1}} \tag{8}$$

$$\omega_{tz2} = \frac{1}{\sqrt{L_2C_2}}. \tag{9}$$

B. Frequency-Selective Cell

The passive resonant topologies introduced in the previous subsection are used within frequency-selective cells to create lossless responses in the active BPFs, as shown in Fig. 1. In order to demonstrate the operating principles of the frequency-selective cell, an ideal circuit schematic that uses Topology A as its resonant element is shown in Fig. 4. The element was designed for a center frequency of 8 GHz. The circuit also comprises three dc bias voltages (V_1, V_2, and V_3) that are fed through ideal high-valued inductors, L_{DC}, that permit the flow of dc currents but reject the high-frequency signals. Moreover, a high-valued capacitor, C_{block}, is placed in series with the inductor, L, to prevent it from grounding the drain of the first FET and the gate of the second FET.

To match the input and output of the cell and select the appropriate amount of gain, the biasing point of the active devices needs to be appropriately selected through the parametric analysis while ensuring that the circuit is stable. Fig. 5 shows how the three bias voltages of the cell affect its response when loss is present ($Q = 20$ for the inductor L). As it can be seen, a BPF transfer function is achieved in the forward transmission response ($|S_{21}|$) and the magnitude of the reverse transmission response ($|S_{12}|$) is below -50 dB across the entire frequency range, confirming the nonreciprocal nature of the frequency-selective cells.

Fig. 5(a) shows the effects of V_1, the first FET's gate bias voltage. As it can be seen, this voltage has no effect on the output matching, but it does affect the amount of input matching and the gain with lower voltages leading to higher gains. Next, Fig. 5(b) shows how V_2, the first FET's drain and second FET's gate bias voltage, influences the overall response. It is inversely proportional to the amount of gain and the level of the output matching. It has a slight effect on the input matching. Finally, Fig. 5(c) presents how V_3, the

Authorized licensed use limited to: UNIVERSITY COLLEGE CORK. Downloaded on February 07,2023 at 16:36:24 UTC from IEEE Xplore. Restrictions apply.

This article has been accepted for inclusion in a future issue of this journal. Content is final as presented, with the exception of pagination.

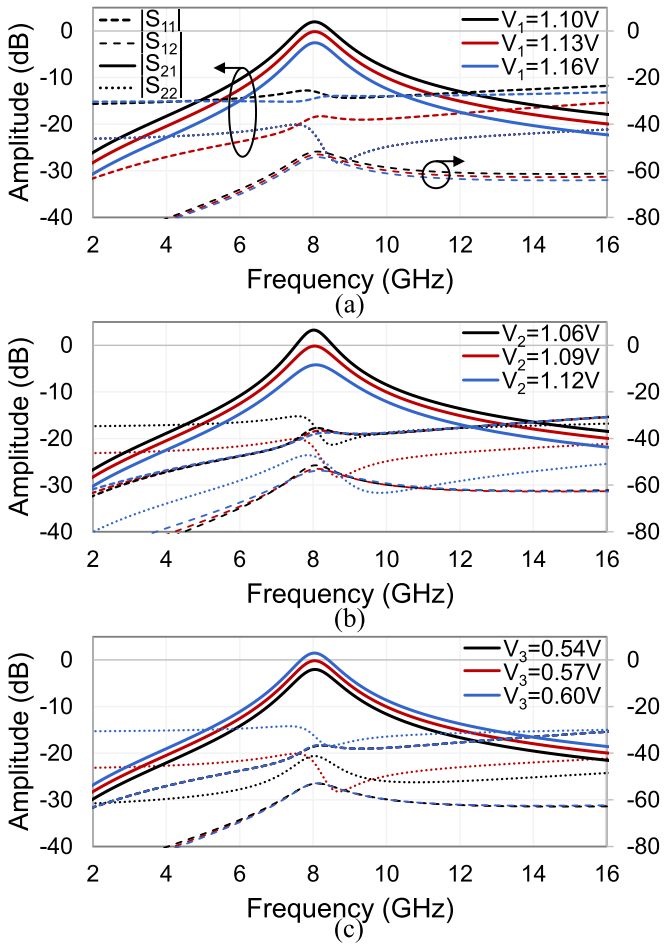


Fig. 5. Simulated power transmission and reflection responses of the circuit schematic in Fig. 4 for $L = 0.117$ nH ($Q = 20$) and $C = 3.2$ pF. (a) Variation of V_1. $V_2 = 1.09$ V and $V_3 = 0.57$ V. (b) Variation of V_2. $V_1 = 1.13$ V and $V_3 = 0.57$ V. (c) Variation of V_3. $V_1 = 1.13$ V and $V_2 = 1.09$ V.

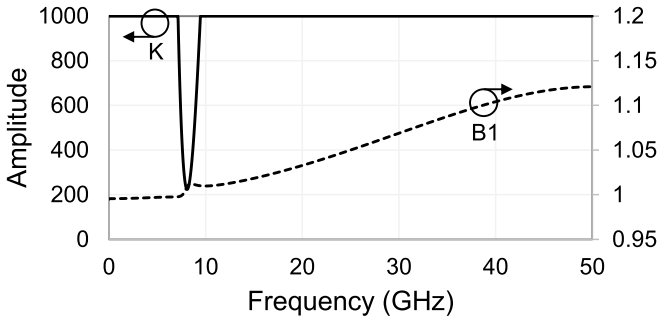


Fig. 6. K- and B1-stability factors of the single-cell circuit in Fig. 4 for $L = 0.117$ nH ($Q = 20$), $C = 3.2$ pF, $V_1 = 1.13$ V, $V_2 = 1.09$ V, and $V_3 = 0.57$ V.

drain bias voltage of the second FET, influences the response. As shown, V_3 does not alter the input matching, but it does change the amount of gain and the output matching. V_3 has less influence on the gain than the other bias voltages. The K- and B1-stability factors for the circuit in Fig. 4 are shown in Fig. 6 and corroborate its stability over the frequency range of 0–50 GHz (i.e., K > 1 and B1 > 0 for the whole range). All FETs used have a size of 2×25 μm.

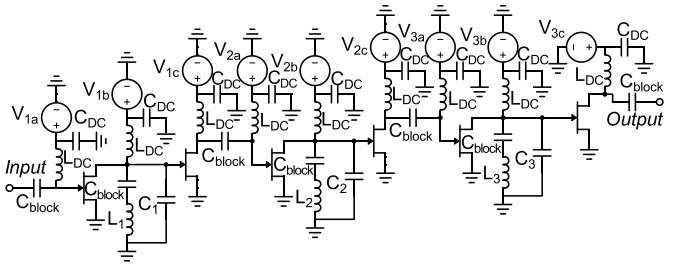


Fig. 7. Circuit schematic of a three-cell actively coupled MMIC BPF ($N = 3$) whose cells consist of Topology A resonant elements.

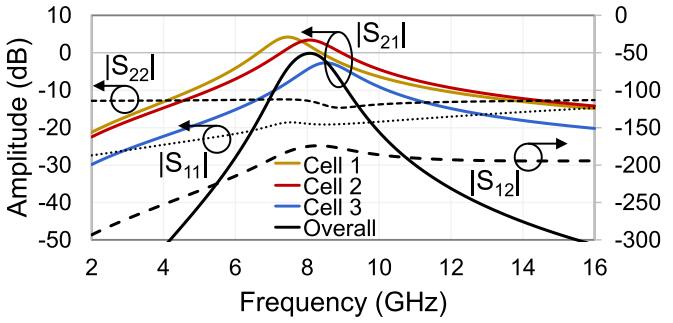


Fig. 8. Transmission and reflection responses of the three different frequency-selective cells and the overall response of the three-cell BPF in Fig. 7. For these responses, $L_1 = 0.116$ nH ($Q = 20$), $C_1 = 3.8$ pF, $L_2 = 0.117$ nH ($Q = 20$), $C_2 = 3.2$ pF, $L_3 = 0.094$ nH ($Q = 20$), $C_3 = 3.6$ pF, $L_{DC} = 100$ nH, $C_{DC} = 10$ pF, $C_{block} = 500$ pF, $V_{1a} = 1.12$ V, $V_{1b} = V_{1c} = V_{2a} = V_{2b} = V_{2c} = V_{3a} = V_{3b} = 1.14$ V, $V_{3c} = 0.65$ V, $I_{1a} = 23.8$ mA, $I_{1b} = 33.8$ mA, $I_{1c} = 32.5$ mA, $I_{2a} = 1.79$ mA, $I_{2b} = 34.3$ mA, $I_{2c} = 32.5$ mA, $I_{3a} = 1.79$ mA, $I_{3b} = 34.2$ mA, and $I_{3c} = 43.8$ mA.

C. BPF Design and Operating Principles

In order to create a filtering transfer function with the frequency-selective cells (i.e., a BPF response), multiple of them are cascaded together. To demonstrate the operating principles of the filter cascade design concept, an ideal, three-cell, active BPF was designed by cascading three cells similar to the ones presented in Section II-B. Specifically, the cells were made with lossy resonant elements (Topology A in Fig. 2(a), L has a Q of 20) and the filter was centered at 8 GHz with a bandwidth (BW) of 1 GHz (i.e., FBW 12.5%). The schematic of the overall filter is shown in Fig. 7. DC-blocking capacitors are added between cells to separate their dc biases. The responses of the filter and its constituent frequency-selective cells are shown in Fig. 8. It can be seen that the reverse transmission ($|S_{12}|$) is simulated to be below -150 dB over the entire frequency range. The K- and B1-stability factors were simulated to confirm unconditional stability in the range of 0–50 GHz.

It can be seen from Fig. 8 that the cells exhibit different center frequencies and amounts of gain. The presented filter architecture differs from conventional designs in terms of the coupling elements between resonators. The resonators of a conventional filter are coupled by passive admittance inverters made of LEs or distributed components (e.g., microstrip) [25]. The type of the realizable transfer function (e.g., Chebyshev and Butterworth) is determined by both the resonator- and coupling-component values. On the

Authorized licensed use limited to: UNIVERSITY COLLEGE CORK. Downloaded on February 07,2023 at 16:36:24 UTC from IEEE Xplore. Restrictions apply.

This article has been accepted for inclusion in a future issue of this journal. Content is final as presented, with the exception of pagination.

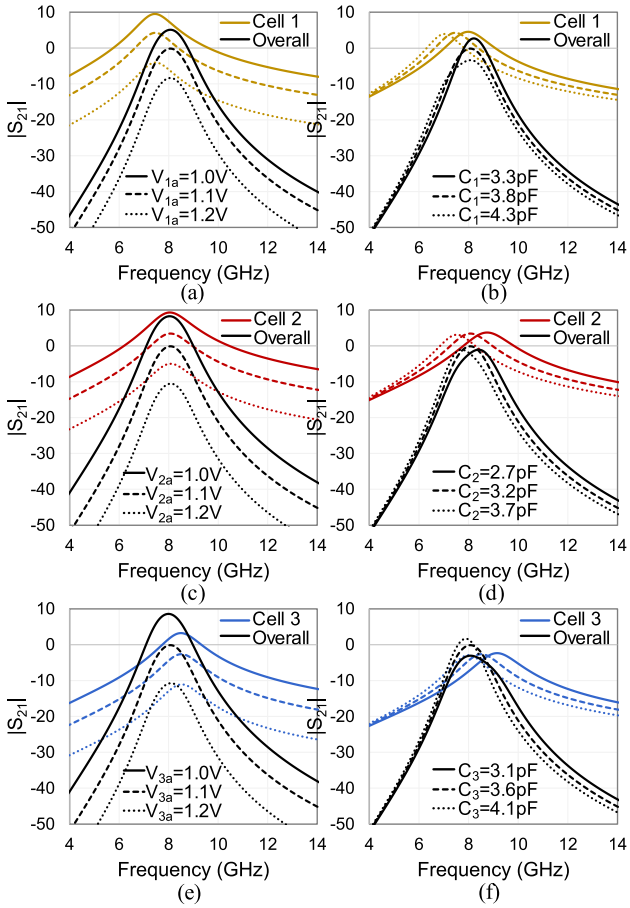


Fig. 9. Simulated transmission responses of the circuit in Fig. 7 and its constituent frequency-selective cells showing variation of the gain and resonant frequency of each cell. The component values are listed in Fig. 8. (a) Variation of the cell 1 gain. (b) Variation of the cell 1 resonant frequency. (c) Variation of the cell 2 gain. (d) Variation of the cell 2 resonant frequency. (e) Variation of the cell 3 gain. (f) Variation of the cell 3 resonant frequency.

other hand, in the proposed active BPF configuration, active devices (i.e., FETs) provide the coupling mechanism between the BPF's resonant elements instead of admittance inverters. In this scenario, only the resonant elements determine the overall transfer function type. Thus, transfer functions with shifted poles (e.g., a Chebyshev response) are produced by shifting the frequencies of the poles resulting from the resonant elements. Although it is difficult to define a filter order in the traditional sense for this BPF, the transfer function selectivity response is comparable to a second-order Butterworth BPF.

A BPF transfer function, such as the one in Fig. 8, is developed by first creating individual frequency-selective cells. The overall response from the cascade of these cells is found by simulating them altogether or by mathematically calculating the response as follows [21]:

$$H(\omega) = H_1(\omega)H_2(\omega), \ldots, H_N(\omega). \tag{10}$$

The desired response is obtained by varying the individual cell parameters (i.e., resonant frequency and gain) by either tuning or optimization. To demonstrate how the cell parameters affect the overall transfer function, the center frequency and gain of each cell are varied and the resulting responses are shown in Fig. 9. Specifically, Fig. 9 plots both the overall response of the cascade and the response of the cell that is being altered. The gain is tuned through the first bias voltage of a cell and the center frequency is tuned through the value of the capacitor in cell's resonant element. As it can be seen, increasing the gain of any cell increases the amount of gain in the overall response. Changing the center frequency of any cell results in different transfer function shapes, particularly near the passband. Thus, the gain and center frequency of each cell can be varied to achieve a multitude of different transfer functions.

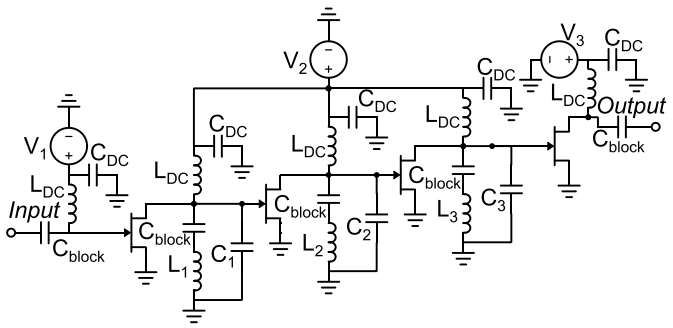


Fig. 10. Simplified circuit schematic of a three-cell actively coupled MMIC BPF ($N = 3$) whose frequency-selective cells consist of Topology A resonant elements. Some dc biases have been connected and cascaded FETs have been removed.

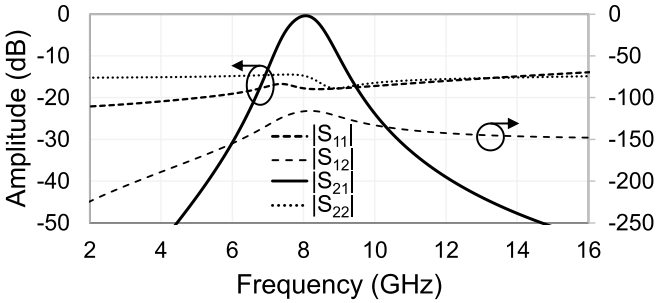


Fig. 11. Simulated power transmission and reflection responses of the BPF in Fig. 10. For this response, $L_1 = 0.116$ nH ($Q = 20$), $C_1 = 3.8$ pF, $L_2 = 0.117$ nH ($Q = 20$), $C_2 = 3.2$ pF, $L_3 = 0.094$ nH ($Q = 20$), $C_3 = 3.6$ pF, $L_{DC} = 100$ nH, $C_{DC} = 10$ pF, and $C_{block} = 500$ pF, $V_1 = 1.11$ V, $V_2 = 1.12$ V, and $V_3 = 0.62$ V.

The schematic in Fig. 7 can be greatly simplified and miniaturized by combining some of the dc biases and removing cascaded FETs. Fig. 10 shows a simplified version of the three-cell schematic where some of the dc biases have been connected and one FET between each connecting set of cells has been removed. Fig. 11 plots the simulated response of the simplified circuit. The transmission response is equivalent to the one in Fig. 8 that resulted from the direct connection of frequency-selective cells. However, the simplified circuit has three dc biases (as opposed to nine) and requires only four FETs (as opposed to six). The component values are the same in the circuits of Figs. 7 and 10, but the dc voltages have been readjusted since some have been connected and some FETs have been removed.

D. Extension to Higher Selectivity and Multi-Band Designs

The other resonant elements in Fig. 2 (i.e., Topologies B and C) can be used in the BPF design to obtain higher

Authorized licensed use limited to: UNIVERSITY COLLEGE CORK. Downloaded on February 07,2023 at 16:36:24 UTC from IEEE Xplore. Restrictions apply.

This article has been accepted for inclusion in a future issue of this journal. Content is final as presented, with the exception of pagination.

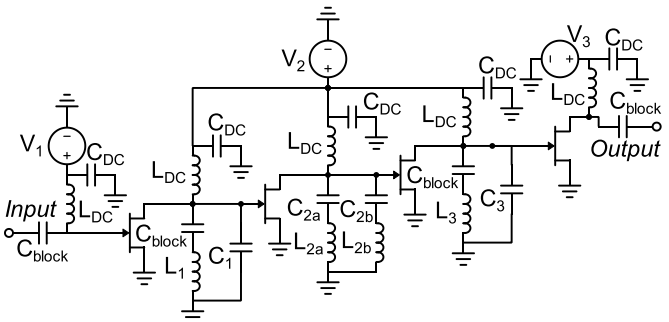


Fig. 12. Simplified circuit schematic of the quasi-elliptic three-cell actively coupled MMIC BPF ($N = 3$) whose frequency-selective cells are made from two Topology A resonant elements and one Topology C resonant element. Some dc biases have been connected and cascaded FETs have been removed.

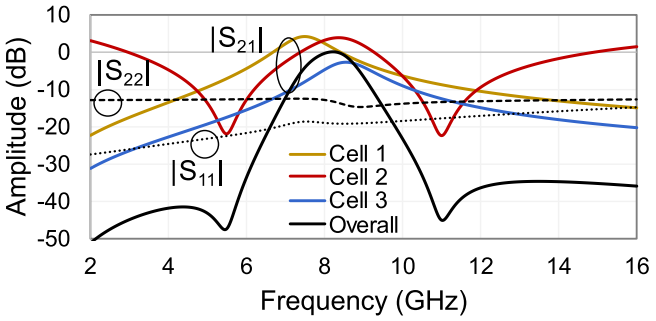


Fig. 13. Transmission and reflection responses of the three different frequency-selective cells and the overall response of the three-cell BPF in Fig. 12. For these responses, $L_1 = 0.116$ nH ($Q = 20$), $C_1 = 3.8$ pF, $L_{2a} = 0.7$ nH ($Q = 20$), $C_{2a} = 1.2$ pF, $L_{2b} = 0.66$ nH ($Q = 20$), $C_{2b} = 0.32$ pF $L_3 = 0.094$ nH ($Q = 20$), $C_3 = 3.6$ pF, $L_{DC} = 100$ nH, $C_{DC} = 10$ pF, $C_{block} = 500$ pF, $V_1 = 1.12$ V, $V_2 = 1.11$ V, $V_3 = 0.62$ V, $I_1 = 23.8$ mA, $I_2 = 99$ mA, and $I_3 = 42.4$ mA.

selectivity or multi-band transfer functions. For example, Topology C introduces TZs to the response (see Fig. 3), which can be used to create quasi-elliptic-type responses. Fig. 12 shows the schematic of a BPF that uses Topology C in its second frequency-selective cell. The schematic was created by replacing the Topology A resonant element in the second cell of the circuit in Fig. 10 with a Topology C resonant element. Its ideally simulated overall and individual cell responses are shown in Fig. 13. As it can be seen, the use of one Topology C resonant elements results in a highly selective response near the passband due to the TZs. The component values and dc voltages were found through tuning to obtain a quasi-elliptic BPF response in the same manner as described in Section II-C. Although the filter order cannot be specified in the traditional sense, its passband exhibits a comparable selectivity to a third-order Butterworth BPF.

Dual-band responses are attained by using Topology B resonant elements in the frequency-selective cells. Fig. 14(a) shows a schematic that contains two cascaded cells that are each made of a Topology B resonant element. Similarly, to the design process described in Section II-C, some of the dc biases have been connected and cascaded FETs have been removed. The BPF in Fig. 14(a) results in two two-pole passbands, as shown in the simulated responses in Fig. 15. The selectivity of the passbands can be further enhanced by

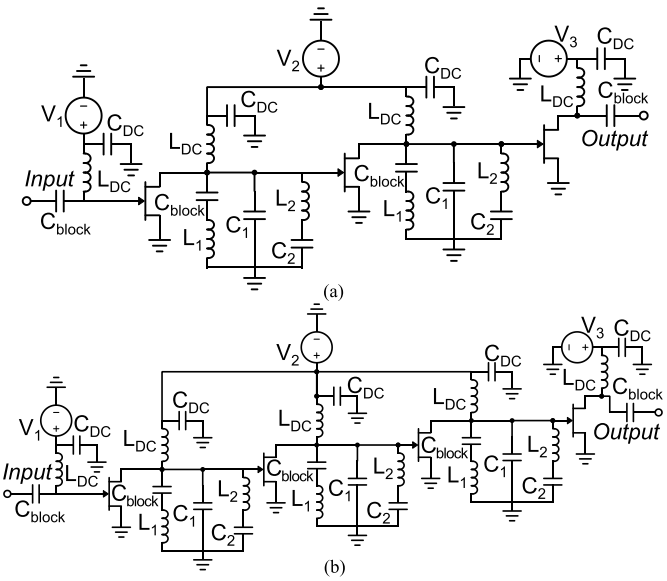


Fig. 14. Simplified circuit schematics of the dual-band actively coupled MMIC BPFs whose frequency-selective cells comprise of Topology B resonant elements. (a) Two-cell schematic ($N = 2$). (b) Three-cell schematic ($N = 3$). Some dc biases have been connected and cascaded FETs have been removed.

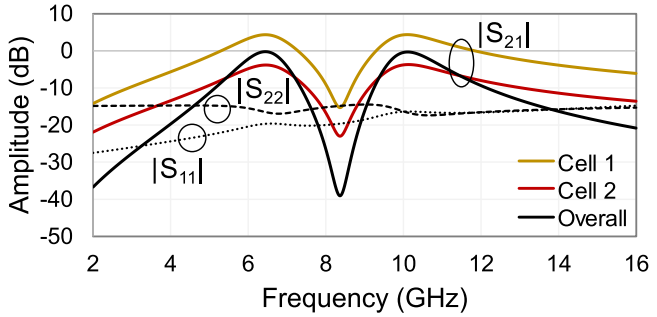


Fig. 15. Transmission and reflection responses of the three different frequency-selective cells and the overall response of the BPF in Fig. 14(a). For these responses, $L_1 = 0.28$ nH ($Q = 20$), $C_1 = 1.38$ pF, $L_2 = 1.39$ nH ($Q = 20$), $C_2 = 0.26$ pF, $L_{DC} = 100$ nH, $C_{DC} = 10$ pF, $C_{block} = 500$ pF, $V_1 = 1.12$ V, $V_2 = 1.13$ V, $V_3 = 0.64$ V, $I_1 = 23.8$ mA, $I_2 = 67.7$ mA, and $I_3 = 43.4$ mA.

cascading additional frequency-selective cells, as demonstrated by the three-cell schematic in Fig. 14(b) and its simulated response in Fig. 16. The use of additional cells to enhance the selectivity of the response is also applicable to any of the previously shown active BPFs.

E. RF Tuning and Varactor Diode Design

The frequency-selective cell can be made frequency tunable by replacing the capacitor(s) in the resonant element with a varactor diode and supporting biasing circuitry, as shown in Fig. 17. A varactor diode can be created in an MMIC platform by connecting the drain and source of an FET and grounding the gate. The drain–source connection operates as the cathode and the gate operates as the anode. The varactor is reversed biased by applying a positive dc voltage, V_T, to its cathode. Fig. 18 shows the schematic of a frequency-tunable, three-cell, active BPF. Its design is based on the schematic

Authorized licensed use limited to: UNIVERSITY COLLEGE CORK. Downloaded on February 07,2023 at 16:36:24 UTC from IEEE Xplore. Restrictions apply.

This article has been accepted for inclusion in a future issue of this journal. Content is final as presented, with the exception of pagination.

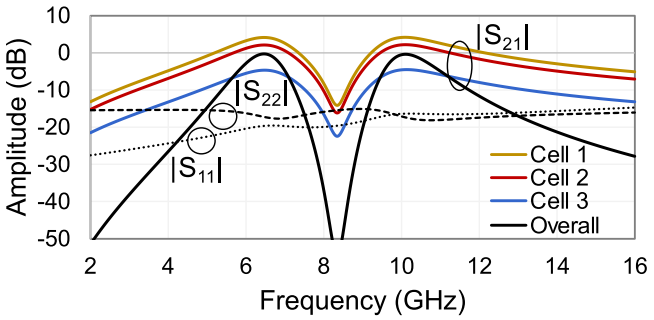


Fig. 16. Transmission and reflection responses of the three different frequency-selective cells and the overall response of the BPF in Fig. 14(b). For these responses, $L_1 = 0.32$ nH ($Q = 20$), $C_1 = 1.18$ pF, $L_2 = 1.65$ nH ($Q = 20$), $C_2 = 0.22$ pF, $L_{DC} = 100$ nH, $C_{DC} = 10$ pF, $C_{block} = 500$ pF, $V_1 = 1.12$ V, $V_2 = 1.14$ V, $V_3 = 0.64$ V, $I_1 = 23.8$ mA, $I_2 = 102.6$ mA, and $I_3 = 43.6$ mA.

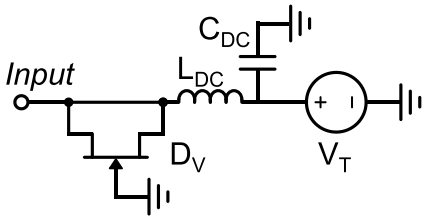


Fig. 17. Varactor diode circuit that can be used to replace C in Fig. 4 to make the frequency-selective cell tunable in terms of center frequency.

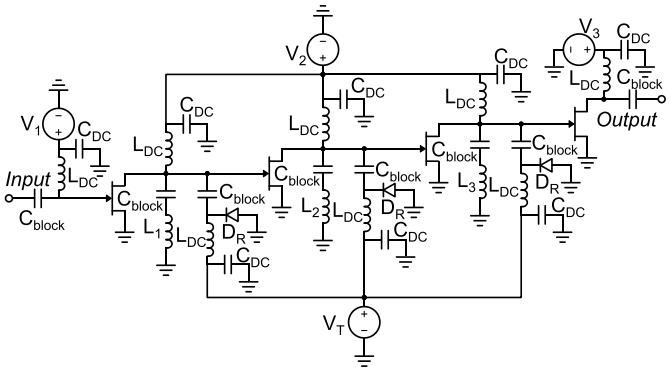


Fig. 18. Simplified circuit schematic of the tunable three-cell actively coupled MMIC BPF ($N = 3$) whose frequency-selective cells comprise Topology A resonant elements with the capacitors replaced by the varactor diode circuit in Fig. 17. Some dc biases have been connected and cascaded FETs have been removed for simplicity and size compactness.

in Fig. 10 where the resonant element capacitors (C_1, C_2, and C_3) have been replaced with the varactor diode and bias circuit in Fig. 17.

The design studies of the varactor diode in Fig. 17 are plotted in Fig. 19. Its design parameters are the number of fingers in the FET, F, its gate width, W, and the bias voltage, V_T. As either F or W is increased, the capacitance also increases and Q decreases. Fig. 19(c) shows that as V_T increases, the capacitance decreases and Q increases. This verifies that this particular FET configuration acts as a varactor diode and can be used to tune the circuit.

F. MMIC Lumped-Element Design

When implementing the LEs in a GaAs MMIC platform, various design tradeoffs must be considered for each

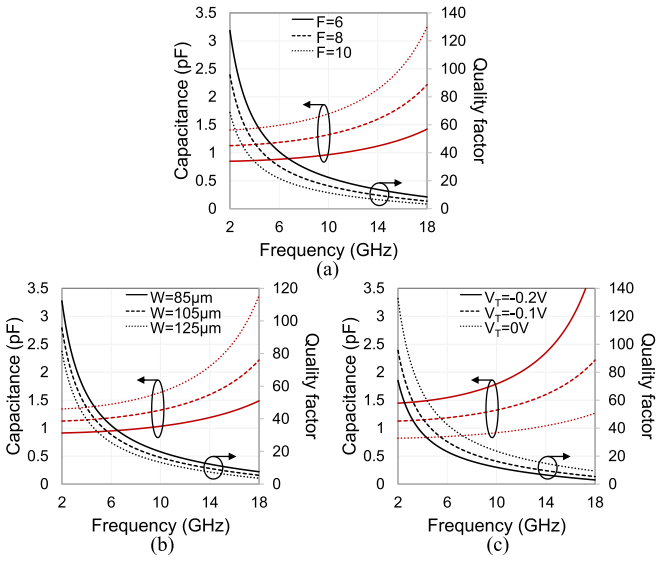


Fig. 19. Varactor diode design studies based on the schematic in Fig. 17. (a) Variation of the number of gate fingers, F. (b) Variation of the gate width, W. (c) Variation of the bias voltage, V_T.

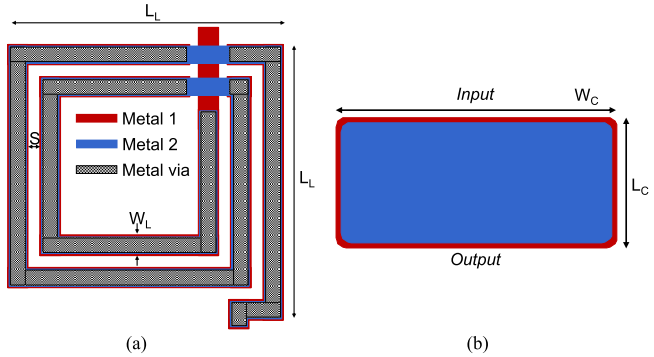


Fig. 20. Layout and EM model of lumped components in a two-metal layer MMIC stack-up. (a) Square inductor. (b) Capacitor.

component (i.e., the inductors and capacitors). The LEs were designed using a two-metal layer MMIC stack-up using the software package AXIEM from Cadence Design Systems and the GaAs process design kit.

The layout of a designed square inductor is shown in Fig. 20(a). Its inductance and Q are plotted against its physical dimensions in Fig. 21. Specifically, the conductor width, W_L, is varied in Fig. 21(a). As W_L is increased, the inductance decreases, but Q increases. Similarly, the separation between loops, S, is proportional to Q but inversely proportional to the inductance, as shown in Fig. 21(b). The number of loops, P, is changed in Fig. 21(c), which demonstrates that it strongly affects the level of inductance with more loops leading to higher values. Finally, Fig. 21(d) shows that the length of the inductor, L_L, also strongly correlates to its inductance.

A model of a capacitor is shown in Fig. 20(b). Its parameter design studies are shown in Fig. 22. In Fig. 22(a), the width of the capacitor, W_C, is varied, and in Fig. 22(b), its length, L_C, is changed. As to be expected, as either dimension is increased, the capacitance is increased. As the width is increased, the maximum Q also increased. Moreover,

Authorized licensed use limited to: UNIVERSITY COLLEGE CORK. Downloaded on February 07,2023 at 16:36:24 UTC from IEEE Xplore. Restrictions apply.

This article has been accepted for inclusion in a future issue of this journal. Content is final as presented, with the exception of pagination.

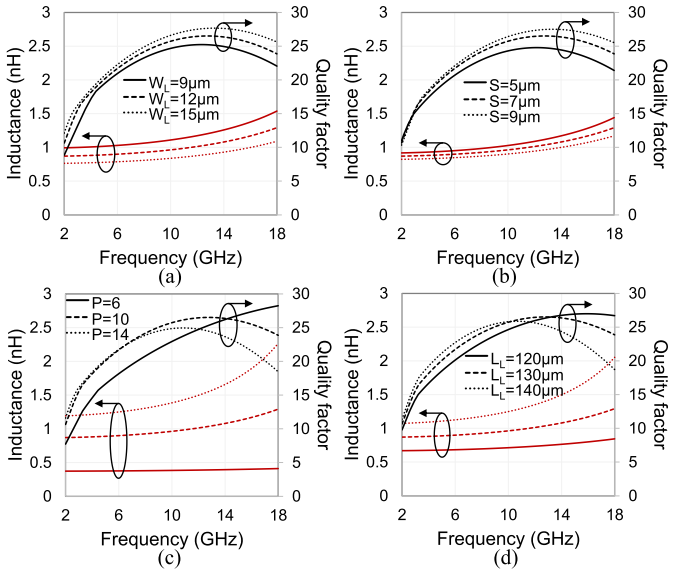


Fig. 21. Square-inductor design studies based on the model in Fig. 20(a). (a) Variation of the conductor width, W_L. (b) Variation of the spacing between loops, S. (c) Variation of the number of loops, P. (d) Variation of the inductor length, L_L.

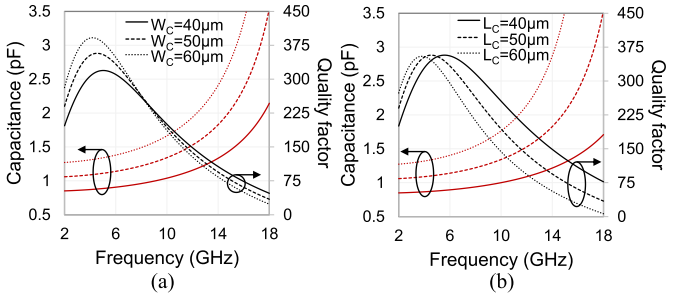


Fig. 22. Capacitor design studies based on the model in Fig. 20(b). (a) Variation of the capacitor width, W_C. (b) Variation of the capacitor length, L_C.

as the length is increased, the frequency of the maximum Q decreases.

III. Experimental Results

Four GaAs MMIC prototypes were designed, manufactured, and tested at the X-band using the commercially available GaAs process PIH-110 from WIN Semiconductors. They include a static quasi-elliptic BPF with two TZs, two static dual-band BPFs, and a tunable BPF, all centered at 8 GHz. The prototypes were developed using the design methodology in Section II. They were implemented in the two-metal layer MMIC stack-up using the software AXIEM from Cadence Design Systems. The RF characterization of the prototypes was performed via on-wafer GSG-probed measurements using a vector network analyzer that was calibrated using an off-chip SOLT calibration kit. As such, the loss and effects of the GSG launching pads are included within the measurements. All measurements were verified to be stable in the frequency range of 0–18 GHz using the K- and B1-stability factors.

A. Quasi-Elliptic BPF

A quasi-elliptic-type three-cell BPF was designed, manufactured, and tested in order to showcase the use of the Topology C resonant element. It was designed by cascading three cells, the first and third cell comprise Topology A resonant elements, whereas the second is implemented by a Topology C one. The schematic of the prototype is shown in Fig. 12 and its photograph is presented in Fig. 23. The quasi-elliptic BPF prototype and its RF-measured and EM-simulated responses are shown in Fig. 24. As shown, they are in good agreement with each other, successfully validating the actively coupled MMIC filter design concept. Its measured center frequency and BW are 7.8 and 1.04 GHz (13.3%), respectively. It can be seen that the introduced TZs increase the out-of-band rejection near the passband, verifying the use of the Topology C resonant element. The measured linearity in terms of one- and two-tone measurements at a frequency of 7.8 GHz is shown in Fig. 25. The separation of the two tones in the two-tone measurement is 10 MHz. The prototype's output-referred 1-dB compression point (P_{1dB}) and third-order intercept (OIP3) are measured to be −5.8 and −3.9 dBm, respectively.

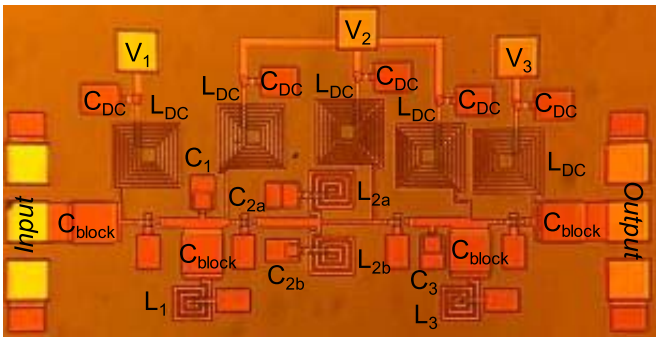


Fig. 23. Photograph of the quasi-elliptic three-cell BPF prototype. The simulated component values are: L_{DC} = 10.6 nH, C_{DC} = 2.6 pF, C_{block} = 4.1 pF, L_1 = L_3 = 0.41 nH, L_{2a} = 0.72 nH, L_{2b} = 0.72 nH, C_1 = C_3 = 0.67 pF, C_{2a} = 1.05 pF, and C_{2b} = 0.29 pF.

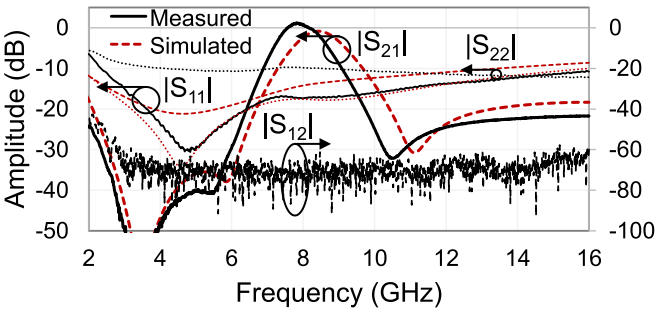


Fig. 24. RF-measured and EM-simulated power transmission and reflection responses of the three-cell quasi-elliptic BPF prototype in Fig. 23.

B. Dual-Band BPFs

Two dual-band (two-cell and three-cell) BPFs were designed, manufactured, and measured. Topology B resonant elements were employed in their design. Their schematics are shown in Fig. 14 and the photographs of the prototypes are shown in Figs. 26 and 27. The dual-band BPFs' RF-measured and EM-simulated responses are shown in Fig. 28. In particular, Fig. 28(a) shows the two-cell prototype's responses. The measured transfer function has bands centered at 6.58 and

Authorized licensed use limited to: UNIVERSITY COLLEGE CORK. Downloaded on February 07,2023 at 16:36:24 UTC from IEEE Xplore. Restrictions apply.

This article has been accepted for inclusion in a future issue of this journal. Content is final as presented, with the exception of pagination.

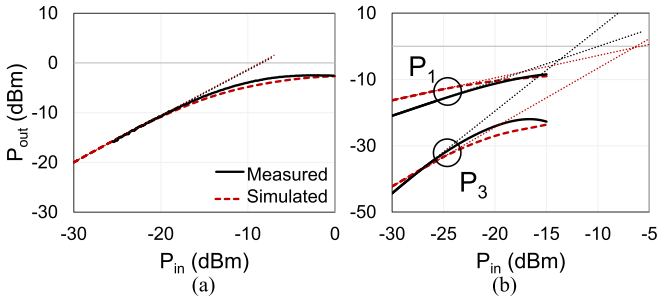


Fig. 25. RF-measured output power as a function of input power for the quasi-elliptic prototype in Fig. 23 at a fundamental frequency of 7.8 GHz. (a) One-tone measurement. (b) Two-tone measurement showing the fundamental frequency (P_1) and the third-order harmonic (P_3).

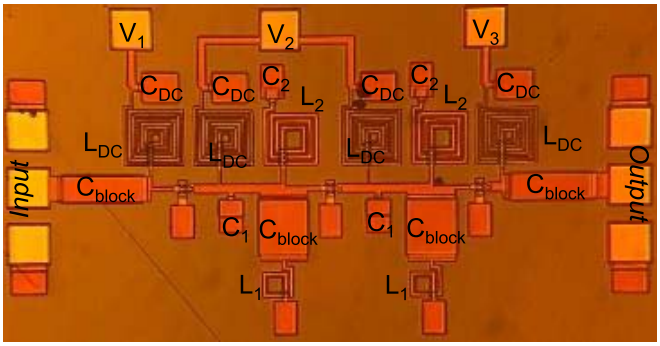


Fig. 26. Photograph of the two-cell dual-band BPF prototype. The simulated component values are: $L_{DC} = 6$ nH, $C_{DC} = 2.6$ pF, $C_{block} = 5.6$ pF, $L_1 = 0.15$ nH, $L_2 = 1.4$ nH, $C_1 = 0.95$ pF, and $C_2 = 0.23$ pF.

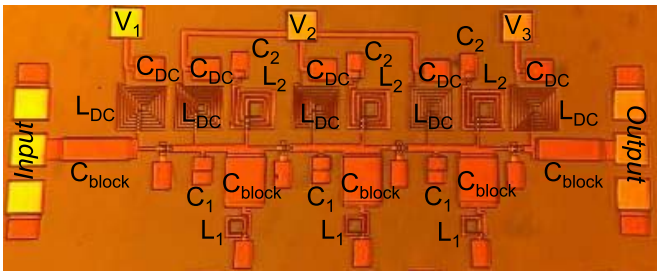


Fig. 27. Photograph of the three-cell dual-band BPF prototype. The simulated component values are: $L_{DC} = 6$ nH, $C_{DC} = 2.6$ pF, $C_{block} = 5.6$ pF, $L_1 = 0.15$ nH, $L_2 = 1.4$ nH, $C_1 = 0.95$ pF, and $C_2 = 0.23$ pF.

9.6 GHz, which have BWs of 0.71 GHz (10.8%) and 0.92 GHz (9.6%), respectively. The measured P_{1dB}'s are -6.7 and -5.2 dBm, respectively, measured at the BPF's center frequencies. Moreover, the measured OIP3s are -5.3 and -1.5 dBm. As it can be seen in Fig. 28(b), the three-cell prototype results in a more selective frequency response than its two-cell counterpart. The center frequencies of the three-stage BPF are measured to be 6.6 and 9.7 GHz. Their respective BWs are 0.5 GHz (7.6%) and 0.89 GHz (9.2%). The first band has a measured P_{1dB} of -6.4 dBm and OIP3 of -4.6 dBm. They were measured at 6.6 GHz. The second band has a measured P_{1dB} of -5.3 dBm and OIP3 of -2.2 dBm, which were measured at 9.7 GHz. These prototypes verify that the active BPF concept can be used to create multi-band transfer functions. Furthermore, they show that cascading additional cells results in higher selectivity transfer functions.

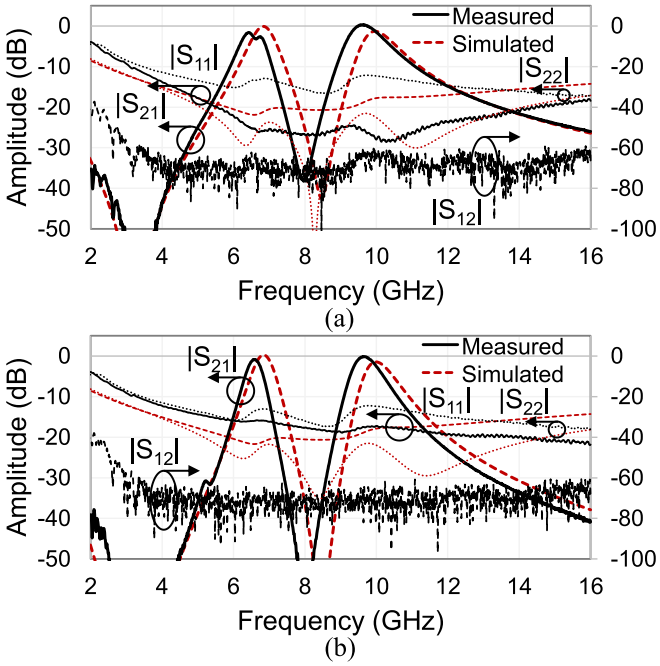


Fig. 28. RF-measured and EM-simulated power transmission and reflection responses of the dual-band active MMIC BPF prototypes that use Topology B frequency-selective cells. (a) Responses from the two-cell prototype in Fig. 26. (b) Responses from the three-cell prototype in Fig. 27.

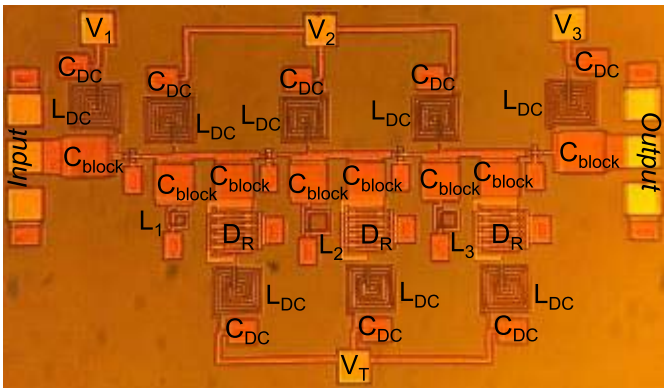


Fig. 29. Photograph of the tunable three-cell BPF prototype. The simulated component values are: $L_{DC} = 6$ nH, $C_{DC} = 2.6$ pF, $C_{block} = 6.7$ pF, $L_1 = 0.12$ nH, $L_2 = 0.2$ nH, and $L_3 = 0.16$ nH.

C. Tunable Three-Cell BPF

The tunable three-cell BPF prototype is made of Topology A resonant elements. Tunability is implemented by replacing the capacitors in the resonant elements with the varactor diode circuit shown in Fig. 17. The overall schematic of the filter is shown in Fig. 18. A photograph and its component values are given in Fig. 29. Fig. 30(a) shows a comparison between the RF-measured and the EM-simulated responses. The BPF has a center frequency of 8.18 GHz and a minimum in-band IL of 0.36 dB. The measured BW is 1.08 GHz (13.2%). Fig. 30(b) shows the filter's tuning ability while altering the dc bias on the varactor diode. It can be tuned in the range of 6.08–9.98 GHz (i.e., 1.64:1). As the filter is tuned, the BW varies from 0.87 GHz (14.3%) at the lowest frequency to 1.46 GHz (14.6%) at the highest. P_{1dB} for one static state

Authorized licensed use limited to: UNIVERSITY COLLEGE CORK. Downloaded on February 07,2023 at 16:36:24 UTC from IEEE Xplore. Restrictions apply.

This article has been accepted for inclusion in a future issue of this journal. Content is final as presented, with the exception of pagination.

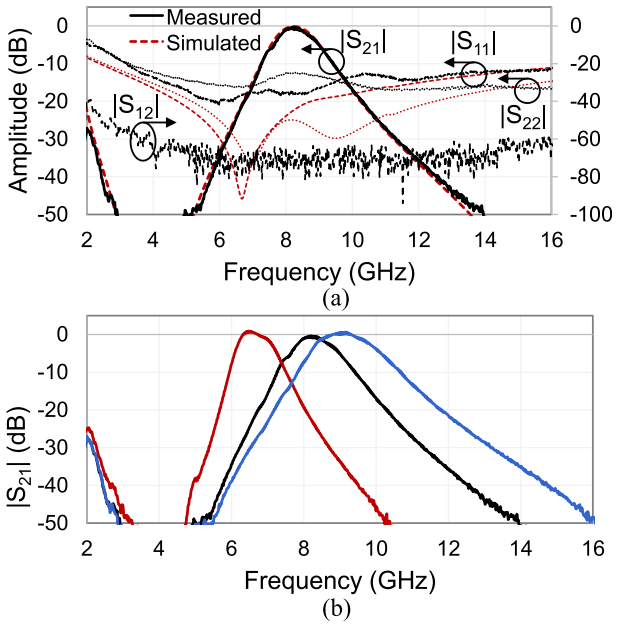


Fig. 30. Three-cell tunable active MMIC BPF prototype based on Topology A resonant elements in Fig. 29. (a) RF-measured and EM-simulated power transmission and reflection responses. (b) Measured center frequency tuning.

TABLE I
COMPARISON WITH OTHER ACTIVE MMIC BPFS

Ref.	f_{cen}, GHz	BW, GHz	N	TZs	IS, dB	P_{DC}, mW	P_{1dB}, dBm	OIP3, dBm	Type/Tech
[6]	3	0.6	3	2	x	x	x	x	Filter-amp. Cascade GaAs
[12]	1.9-2.4 (1.26:1)	0.06	1	0	x	63	-21	x	Recursive Silicon
[13]	1.2-1.3 (1.08:1)	0.04	2	0	x	x	x	x	Recursive GaAs
[18]	14.6-15.4 (1.06:1)	0.06	1	0	x	x	x	x	Negative resistance GaAs
[19]	2.2-2.4 (1.09:1)	0.3	6	0	x	25	~ -20	x	Negative resistance GaAs
[21]	10.6-12.8 (1.21:1)	1.2	3	0	x	x	x	x	Active coupling GaAs
[22]	11	1.5	3	0	x	x	x	x	Active coupling GaAs
Quasi-elliptic	7.8	1.0	3	2	60	141	-5.8	-3.9	Active coupling GaAs
Dual-band A	6.6 9.6	0.7 0.9	2	2	60	91	-6.7 -5.2	-5.3 -1.5	Active coupling GaAs
Dual-band B	6.6 9.7	0.5 0.9	3	3	60	140	-6.4 -5.3	-4.6 -2.2	Active coupling GaAs
Tunable	6.1-10 (1.64:1)	0.9-1.5	3	0	60	135	-7.5	-2.5	Active coupling GaAs

N – Number of transmission poles, IS – minimum in-band isolation in reverse transmission direction, x – not given, P_{DC} – DC power consumption.

is −7.5 dBm, while the OIP3 is measured to be −2.5 dBm. These were measured at 8 GHz.

D. Comparison With State of the Art

Table I compares the active MMIC BPFs presented in this article to state-of-the-art (SOA) active MMIC BPFs. As it can be seen, the proposed filter design concepts outperform the SOA in a number of categories. Specifically, the proposed tunable three-cell has the widest tuning range of all other active MMIC BPFs. Moreover, a multi-band, active BPF configuration is shown for the first time in this work. The proposed BPFs are also among the most selective with the three-cell quasi-elliptic filter having two TZs and exhibiting the highest output-referred 1-dB compression point.

IV. CONCLUSION

A new class of active-type MMIC BPFs alongside a simple RF design methodology have been presented in this article. They are based on in-series cascaded cells that each consists of two FETs and a resonant element. The FETs actively couple resonant elements together and counteract the loss of the passive components. Furthermore, the unilateral nature of the FETs produces a nonreciprocal response in the overall filter architecture allowing to embed the codesigned function of an RF isolator within a filter, thus reducing the overall size of the RF front end. A variety of transfer function types such as multi-band and quasi-elliptic are possible by utilizing different types of resonant elements. The cascaded resonant element BPF concept was analyzed through studies on one- and three-cell ideal filters. For experimental demonstration purposes, four MMIC prototypes were generated and measured at the X-band. They include a tunable three-cell BPF, two dual-band BPFs, and a quasi-elliptic BPF.

ACKNOWLEDGMENT

The authors would like to thank WIN Semiconductors for providing access to their PIH-110 process and for manufacturing the filters.

REFERENCES

[1] L. Pantoli, G. Leuzzi, F. Deborgies, P. Jankovic, and F. Vitulli, "A survey of MMIC active filters," *Electronics*, vol. 10, no. 14, p. 1680, Jul. 2021.
[2] Z. Sun, Y. Zhou, and C. Cheng, "A GaAs-based bandpass filter with tiny size and high-order quasi-elliptic function response," in *Proc. Int. Appl. Comput. Electromagn. Soc. Symp. China (ACES)*, Aug. 2019, pp. 1–2.
[3] Q. Sun, J. Yuan, J. Lu, A. Rezazadeh, L. Krishnamuthy, and V. T. Vo, "Compact multilayer CPW MMIC spiral directional couplers and band-pass filters," in *Proc. 40th Eur. Microw. Conf.*, 2010, pp. 561–564.
[4] Y. Chen, B. Deng, L. Sun, B. Wang, and J. Chen, "A compact 1.8–3.0 GHz IPD-based wideband bandpass filter for System-on-Package," in *IEEE MTT-S Int. Microw. Symp. Dig.*, May 2019, pp. 1–3.
[5] Z. Wu, Y. Shim, and M. Rais-Zadeh, "Miniaturized UWB bandpass filters integrated with notch filters using a silicon-based integrated passive device technology," in *IEEE MTT-S Int. Microw. Symp. Dig.*, Jun. 2011, pp. 1–4.
[6] F.-J. Chen, X. Cheng, L. Zhang, Y.-L. Tian, Y. Tang, and X.-J. Deng, "Synthesis and design of lumped-element filters in GaAs technology based on frequency-dependent coupling matrices," *IEEE Trans. Microw. Theory Techn.*, vol. 67, no. 4, pp. 1483–1495, Apr. 2019.
[7] M. Rais-Zadeh, J. T. Fox, D. D. Wentzloff, and Y. B. Gianchandani, "Reconfigurable radios: A possible solution to reduce entry costs in wireless phones," *Proc. IEEE*, vol. 103, no. 3, pp. 438–451, Mar. 2015.
[8] B. Mini-Circuits, "Reflectionless filters improve linearity and dynamic range," *Microw. J.*, vol. 58, no. 8, pp. 42–50, Aug. 2015.
[9] D. Simpson and D. Psychogiou, "X-band quasi-reflectionless MMIC bandpass filters with minimum number of components," *IEEE Trans. Electron Devices*, vol. 68, no. 9, pp. 4329–4334, Sep. 2021.
[10] M. A. Morgan and T. A. Boyd, "Reflectionless filter structures," *IEEE Trans. Microw. Theory Techn.*, vol. 63, no. 4, pp. 1263–1271, Apr. 2015.

Authorized licensed use limited to: UNIVERSITY COLLEGE CORK. Downloaded on February 07,2023 at 16:36:24 UTC from IEEE Xplore. Restrictions apply.

This article has been accepted for inclusion in a future issue of this journal. Content is final as presented, with the exception of pagination.

[11] B. K. Kormanyos, T. K. Quach, P. L. Orlando, A. G. Mattamana, and K. S. Groves, "26 GHz on chip cascaded filter using low *Q* inductors," in *IEEE MTT-S Int. Microw. Symp. Dig.*, May 2010, pp. 1744–1747.
[12] S. Darfeuille et al., "Silicon-integrated 2-GHz fully-differential tunable recursive filter for MMIC three-branch channelized bandpass filter design," in *IEEE MTT-S Int. Microw. Symp. Dig.*, Jun. 2006, pp. 776–779.
[13] H. Suwaki and T. Ohira, "A very small MMIC variable filter based on a new active filter design concept," in *Proc. 12th Annu. Symp. Gallium Arsenide Integr. Circuit (GaAs IC)*, 1990, pp. 93–96.
[14] M. J. Schindler and Y. Tajima, "A novel MMIC active filter with lumped and transversal elements," *IEEE Trans. Microw. Theory Techn.*, vol. 37, no. 12, pp. 2148–2153, Dec. 1989.
[15] L. Pantoli, V. Stornelli, G. Leuzzi, L. Hongjun, and H. Zhifu, "GaAs MMIC tunable active filter," in *Proc. Integr. Nonlinear Microw. Millim.-Wave Circuits Workshop (INMMiC)*, Apr. 2017, pp. 1–3.
[16] U. Karacaoglu and I. D. Robertson, "MMIC active bandpass filter using negative resistance elements," in *IEEE MTT-S Int. Microw. Symp. Dig.*, May 1995, pp. 135–138.
[17] M. Ito, K. Maruhashi, S. Kishimoto, and K. Ohata, "60-GHz-band coplanar MMIC active filters," *IEEE Trans. Microw. Theory Techn.*, vol. 52, no. 3, pp. 743–750, Mar. 2004.
[18] S. Dardillac, D. Eyllier, L. Billonnet, and B. Jarry, "Active impedance profile technique for selective tuneable active filter with gain," in *IEEE MTT-S Int. Microw. Symp. Dig.*, Jun. 2005, pp. 791–794.
[19] R. Kaunisto, P. Alinikula, K. Stadius, and V. Porra, "A low-power HBT MMIC filter based on tunable active inductors," *IEEE Microw. Guided Wave Lett.*, vol. 7, no. 8, pp. 209–211, Aug. 1997.
[20] L. Pantoli, V. Stornelli, G. Leuzzi, H. Li, and Z. Hu, "On-chip active filter in GaAs technology for wireless communication systems," *Anal. Integr. Circuits Signal Process.*, vol. 96, no. 1, pp. 1–7, Jul. 2018.
[21] F. Bergeras, P. Duême, J. Plaze, L. Darcel, B. Jarry, and M. Campovecchio, "Novel MMIC architectures for tunable microwave wideband active filters," in *IEEE MTT-S Int. Microw. Symp. Dig.*, May 2010, pp. 1356–1359.
[22] L. Darcel, P. Duême, R. Funck, and G. Alquié, "New MMIC approach for low noise high order active filters," in *IEEE MTT-S Int. Microw. Symp. Dig.*, Jun. 2005, pp. 787–790.
[23] L. Darcel, P. Duême, R. Funck, and G. Alquié, "A new methodology for achieving MMIC bandpass active filters at high frequencies," in *Proc. Gallium Arsenide Appl. Symp.*, 2004, pp. 87–90.
[24] R. R. Bonetti and A. E. Williams, "An octave-band MMIC active filter," in *IEEE MTT-S Int. Microw. Symp. Dig.*, May 1990, pp. 823–826.
[25] J.-S. Hong, *Microstrip Filters for RF/Microwave Applications*, 2nd ed. New York, NY, USA: Wiley, 2011.



Dakotah Simpson (Member, IEEE) received the B.S. degree in electrical engineering from the South Dakota School of Mines and Technology, Rapid City, SD, USA, in 2017, and the M.S. and Ph.D. degrees in electrical engineering from the University of Colorado Boulder, Boulder, CO, USA, in 2020 and 2022, respectively.

He is currently an RF Engineer at Lockheed Martin Space, Denver, CO, USA. His research interests included the design, characterization, and synthesis of reconfigurable RF/microwave single-ended and balanced filters and frequency-selective feed networks for linear antenna arrays.

Mr. Simpson is a member of the IEEE Microwave Theory and Techniques Society (IEEE MTT-S) and the Applied Computational Electromagnetics Society (ACES). He was a recipient of the MTT-S 2018 Graduate Fellowship, the University of Colorado's Dean's Graduate Assistantship and the ECEE Gold Award for Research, and the 2018–2019 Lockheed Martin Endowed Graduate Fellowship. He received the first place prize at the 2018 IMS Student Design Competition and 2018 EuMW Student Design Competition and the second place prize at the 2019 IMS Student Design Competition.



Dimitra Psychogiou (Senior Member, IEEE) received the Dipl.-Eng. degree in electrical and computer engineering from the University of Patras, Patras, Greece, in 2008, and the Ph.D. degree in electrical engineering from the Swiss Federal Institute of Technology (ETH), Zürich, Switzerland, in 2013.

She is currently a Professor of electrical and electronic engineering with the University College Cork (UCC), Cork, Ireland, and the Tyndall National Institute, Cork. Prior to joining UCC, she was a Senior Research Scientist with Purdue University, West Lafayette, IN, USA, and an Assistant Professor with the University of Colorado Boulder, Boulder, CO, USA. Her research has been presented in more than 160 IEEE publications. Her current research interests include RF design and characterization of reconfigurable microwave and millimeter-wave passive components, RF MEMS, acoustic wave resonator-based filters, tunable filter synthesis, and frequency-agile antennas.

Prof. Psychogiou is a Senior Member of URSI and a member of the IEEE MTT-S Filters and Passive Components (MTT-5) and Microwave Control Materials and Devices (MTT-13) committees. Furthermore, she serves on the Technical Review Board for various IEEE and EuMA conferences and journals. She received the 2020 CAREER Award from the National Science Foundation (NSF), the 2020 URSI Young Scientist Award, and the Junior Faculty Outstanding Research Award from UC Boulder. She is also the Chair of MMT-13 and the Secretary of USNC-URSI Commission D. She is also an Associate Editor of the IEEE MICROWAVE AND WIRELESS COMPONENTS LETTERS and the *International Journal of Microwave and Wireless Technologies*. Previously, she was an Associate Editor of the *IET Microwaves, Antennas and Propagation Journal*.

Authorized licensed use limited to: UNIVERSITY COLLEGE CORK. Downloaded on February 07,2023 at 16:36:24 UTC from IEEE Xplore. Restrictions apply.